
The choice of droplet size probability distribution function for oil spill modeling is not trivial

Faillettaz Robin ^{1,2,*}, Paris Claire B. ¹, Vaz Ana C. ¹, Perlin Natalie ¹, Aman Zachary M. ³, Schlüter Michael ⁴, Murawski Steven A. ⁵

¹ University of Miami, Rosenstiel School of Marine and Atmospheric Science, FL 33149, Miami, USA

² Ifremer, STH, F-56100 Lorient, France

³ Centre for Energy, School of Mechanical and Chemical Engineering, The University of Western Australia, Crawley 6009, WA, Australia

⁴ Institute of Multiphase Flows, Hamburg University of Technology, Eißendorfer Straße 38, 21073 Hamburg, Germany

⁵ University of South Florida, College of Marine Science, 140 7th Ave. S., St. Petersburg, FL 33701, USA

* Corresponding author : Robin Faillettaz, email address : robin.faillettaz@ifremer.fr

Abstract :

The droplet size distribution (DSD) formed by gas-saturated oil jets is one of the most important characteristics of the flow to understand and model the fate of uncontrolled deep-sea oil spills. The shape of the DSD, generally modeled as a theoretical lognormal, Rosin-Rammler or non-fundamental distribution function, defines the size and the mass volume range of the droplets. Yet, the fundamental DSD shape has received much less attention than the volume median size (d_{50}) and range of the DSD during ten years of research following the Deepwater Horizon (DWH) blowout. To better understand the importance of the distribution function of the droplet size we compare the oil rising time, surface oil mass, and sedimented and beached masses for different DSDs derived from the DWH literature in idealized and applied conditions, while keeping d_{50} constant. We highlight substantial differences, showing that the probability distribution function of the DSD for far-field modeling is, regardless of the d_{50} , consequential for oil spill response.

Highlights

► The importance of the oil droplet size distribution function was not known. ► The distribution function of the DSD drives the oil mass distribution patterns. ► First response should consider different d_{50} s and probability distribution functions.

Keywords : Droplet size distribution, DSD, Oil spill, Oil spill model, Oil model, Deepwater Horizon, Blowout, d_{50} , Probability distribution function

35 **MAIN TEXT:**

36 The droplets sizes are key characteristics to predict the transport and fate of uncontrolled deep-sea
37 oil spills. The 2010 Deepwater Horizon (DWH) blowout released an estimated five million barrels
38 of live oil into the northern Gulf of Mexico (GoM), impacting the beaches and seafloor (Nixon et al.
39 2016, Romero et al. 2017). Studies had previously focused on the volume median size of oil
40 droplets (d_{50}) to understand its effect on emulsion stability (Tambe and Sharma 1994) and,
41 immediately after the DWH, on the timing and amount of oil surfacing (Ryerson et al. 2012). Ten
42 years later, there is still an ongoing debate on the correct d_{50} of the DWH oil droplets, since the d_{50}
43 estimated at the time of the spill was a decisive factor for the unprecedented use of sub-sea
44 dispersant injection as a response strategy (Paris et al. 2018). Droplet size distribution (DSD)
45 estimates have thus been the focus of numerous analytical models, such as dynamical models (Zhao
46 et al. 2014, 2016, Gros et al., 2017) or equilibrium models with modified Weber number (Johansen
47 et al., 2013, Li et al. 2017) and of laboratory work under normal atmospheric conditions and
48 temperature using the Ohmsett tank (Zhao et al. 2016) and under high-pressure and cold-
49 temperature using sapphire cell and jets experiments with gas-saturated petroleum (Aman et al.,
50 2015, Malone et al. 2018). Improvement to the understanding of DSD in the jet plume and
51 subsurface layer was set as a top priority to inform oil spill models (Malone et al. 2018; Lehr and
52 Socolofsky 2020). However, regardless of the d_{50} , the importance of the fundamental shape, that is
53 the probability distribution function (PDF) of the DSD, on the rise of the oil from deep-sea blowout
54 and on its transport has been, so far, overlooked; our study fills this gap.

55

56 While analytical methods predicted a large range of droplet sizes (up to 2.5 mm, Gros et al. 2017;
57 e.g. Figure 1a), scaled-up laboratory experiments based on turbulent dissipation rates (TDR, Aman
58 et al. 2005; Pesch et al. 2020a) estimated at the Macondo riser-pipe found smaller droplets (<500
59 μm , e.g. Figure 1b), similar to lognormal DSD acquired during the few dive operations in the deep
60 plume (1100 m) and in deeper waters at 1400 m (Li et al. 2015, Spaulding et al., 2015). Regardless
61 of the estimated median droplet size, there is so far no consistency on the PDF of the oil DSD.
62 Although the most commonly assumed PDFs such as lognormal (LN) and Rosin-Rammler (RR) are
63 fairly similar in shape, their distributions' edges drastically differ (Figure 1). Here, we quantify the
64 difference in proportion of oil mass rising at the surface, sedimented on the seafloor, and beached
65 on the shoreline focusing on the importance of the *distribution function* of the droplet size rather
66 than the d_{50} . We generated two hypothetical cases in which oil droplets ranged from 1 to 2400 μm
67 (case 1, $d_{50} = 900 \mu\text{m}$) and from 1 to 500 μm (case 2, $d_{50} = 117 \mu\text{m}$), derived from two published
68 studies which used different droplet models, Gros et al. (2017) and Aman et al. (2015), respectively.
69 We kept the d_{50} and the droplet size ranges similar among cases, which thus only differed by their
70 PDF (Figure 1a,c). For both cases, one dynamic probability distribution function from the
71 simulation model VDROD-J obtained from Gros et al. (2017) was used as baseline, and two
72 theoretical distribution functions, the lognormal and Rosin-Rammler distributions, were fitted to the
73 DSDs from VDROD-J using the R package *fitdistrplus* (Delignette-Muller and Dutang, 2015). The
74 standard deviation and scale parameters were extracted from the lognormal and Rosin-Rammler
75 fits, and used to generate the new lognormal and Rosin-Rammler DSDs. The DSD parameters are:
76 d_{50} set to 900 μm and 117 μm , $\log(\text{SD})$ set to 0.3920 and 0.4297 for the lognormal, and shape set
77 to 3.5010 and 3.3110 for the case 1 and case 2, respectively).

78

79 In a first approach, considering idealized conditions, we estimated the maximum potential effect
80 of the choice of DSD on the rising speed and surfacing time of the oil droplets. We applied an
81 integrated formulation of buoyant velocity from Zheng and Yapa (2000). The critical diameter
82 d_c , beyond which Stokes' law does not apply (i.e., Reynolds number > 1), which is defined as:

83

$$d_c = \frac{9.52\mu^{2/3}}{(g\rho\Delta\rho)^{1/3}}$$

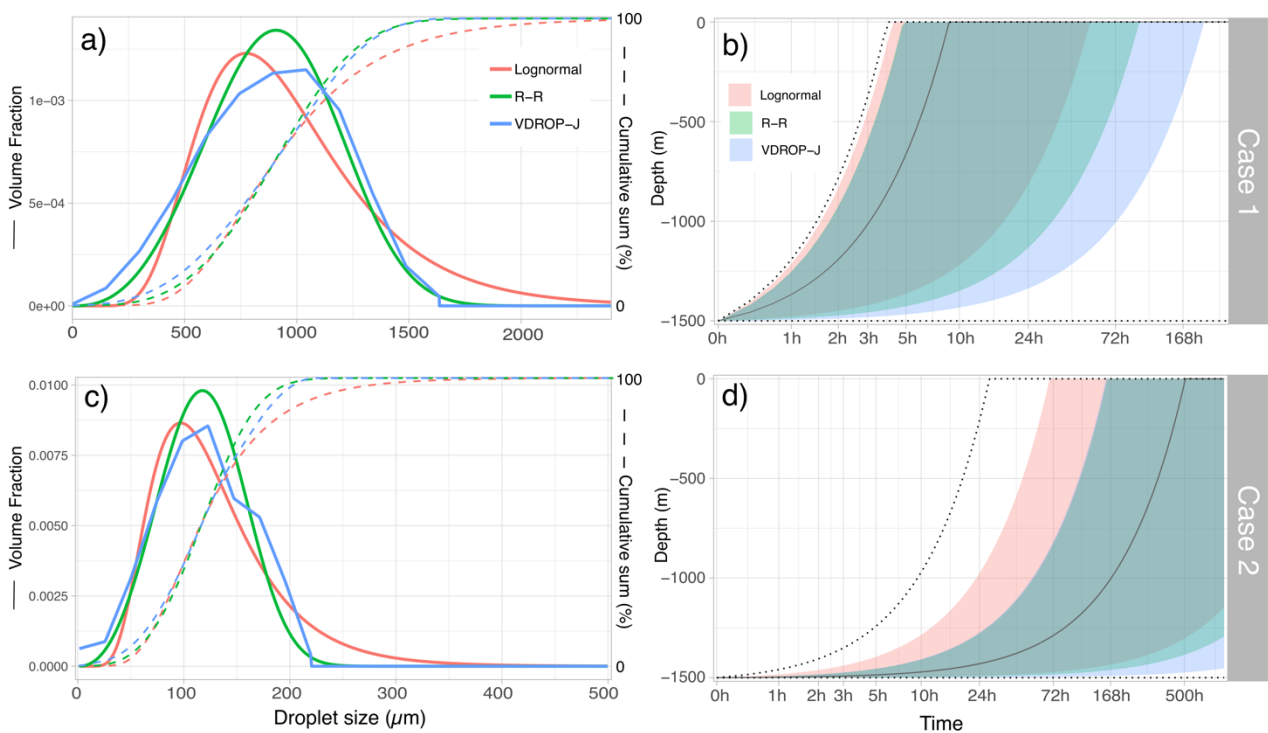
84 where μ is the dynamic viscosity of the ambient fluid, g the gravitational acceleration
 85 ($g=9.8 \text{ m s}^{-2}$), ρ is the ambient fluid density and $\Delta\rho$ is the absolute difference of density between
 86 oil and seawater. If the spherical droplet diameter is smaller than d_c , then the terminal velocity
 87 (U_T) of the droplet is:

$$U_T = \frac{gd^2\Delta\rho}{18\mu}$$

88
 89 When the droplet spherical diameter is larger than d_c , the terminal velocity of droplets is
 90 approximated as:

$$U_T = \left(\frac{8gd\Delta\rho}{3\rho} \right)^{1/2}$$

91



92

93 **Figure 1. Distribution, cumulative sum and timing of surfacing of different analytical,**
 94 **Lognormal and Rosin-Rammler (R-R) droplet size distributions (DSD) fitted on two cases**
 95 **with different d_{50} and size ranges (case 1, size range and d_{50} from Gros et al. 2017 and case 2**
 96 **from Aman et al. 2015). a) Probability distribution functions from VDROp-J (blue) and the fitted**
 97 **lognormal (red) and R-R (green) theoretical distribution laws for the hypothetical case 1 (solid**
 98 **lines) and cumulative sums highlighting that all share the same d_{50} (dashed lines). b) Oil droplets'**
 99 **vertical distribution for the various DSDs when released at the approximate depth (1500 m) and**

100 temperature (4°C) of the Macondo well for the case 1 (upper depth: quantile 99%, solid lines:
101 median, lower depth: quantile 1%) over time (x-axis is log₁₀-transformed). The dashed lines show
102 the minimum and maximum depth of the oil droplets. **c)** and **d)** Same as a) and b) but for case 2.
103 The median droplet depths are similar among PDFs because they have the same d₅₀.

104

105 Differences in the rise velocities of the bulk of the oil were comparable, as expected from the
106 design of the simulations which focused on the tails of the PDFs rather than the d₅₀. However,
107 solely based on the differences between the PDF of the DSD, the rising time of the largest
108 droplets (quantile 99%) differed by up to 17.7% (45 min) for case 1 (Lognormal vs. VDROD-J;
109 Figure 1b), and by as much as 127.1% (88 h) for case 2 (Figure 1d). While for the smallest
110 droplets (quantile 1%), rising time would vary by up to 325.2% (167.5 h) for the case 1 (Figure
111 1b), and by over 5-fold for the case 2 (Figure 1d). The estimated rising velocities of the different
112 quantiles are provided in the Supplementary Information (Table S1). The surfacing time of the
113 lognormal and Rosin-Rammler DSDs from case 1 with a d₅₀ of 900 μm (minimum surfacing
114 time of 4 h, 8.75 h for 50% and 51.55 h for 99% of the oil) matches the estimates without sub-
115 sea dispersant injection (SSDI) at the Macondo wellhead from Testa et al. (2016) and Gros et al.
116 (2017) that suggest that all the oil reached the surface within 7 h for the largest droplets. In our
117 idealized conditions with the same d₅₀, the lower tail of the VDROD-J DSD requires an extra
118 125.25 h to surfacing as compared to the Rosin-Rammler DSD and 167.5 h compared to the
119 lognormal one (Figure 1b). For the case 2, with a d₅₀ of 117 μm, the relative anomalies of
120 surfacing time are higher among the different PDFs due to the wider range of surfacing time
121 compared to case 1. This long surfacing time results from the small d₅₀ and the omission of
122 internal degassing process, whereby the multiphase droplet ascent accelerates as its gas-phase
123 expands with decreasing hydrostatic pressure (Pesch et al. 2018, 2020b). Notably, the lognormal
124 distribution differs the most from the Rosin-Rammler and VDROD-J PDFs (Figure 1b,d). Our
125 idealized conditions results are also in line with the predominating importance of the d₅₀ for the
126 median surfacing time of oil droplets, with longer surfacing time for smaller d₅₀s (Paris et al.

127 2012; Socolofsky et al. 2019), yet they still show that the choice of distribution function has
128 notable influence.

129

130 We then applied the same approach of comparing different outputs by only varying the PDF in a
131 more realistic application to the DWH oil spill. We used a four-dimension Lagrangian
132 framework, the Connectivity Modeling System (CMS; Paris et al. 2013), in which the DSDs are
133 deployed in simulations configured with the DWH initial conditions as described in Perlin et al.
134 (2020). In short, the CMS oil application performs Lagrangian particle tracking of oil droplets
135 released in the far-field at the trap height, approximately 300 m above the wellhead (Socolofsky
136 et al. 2011). Particle transport calculations take into account 3D ocean currents, wind drift,
137 temperature, salinity, multi-fraction droplet density, droplet size evolution due to partitioning
138 and biodegradation, and surface oil evaporation (Paris et al. 2012; Le Henaff et al. 2012; Lindo-
139 Atichati et al. 2016; Perlin et al. 2020). The 4th order Runge-Kutta integration scheme forms the
140 basis for particle advection in the model, while a random walk model represents sub-grid scale
141 turbulent diffusion (Paris et al. 2013). In our simulations, the vertical and horizontal diffusivities
142 coefficients were based on the empirical approximations from Paris et al. (2012) and set to 10^{-5}
143 $\text{m}^2 \text{s}^{-1}$ and $1 \text{m}^2 \text{s}^{-1}$. Computations of the vertical terminal velocity of a droplet are based on its
144 density and size, its Reynolds number, as well as on other ambient conditions such as water
145 temperature, salinity, density, and kinematic viscosity (Zheng et al. 2003, Paris et al. 2012).
146 Fluid flow includes a release of 3000 oil droplets at the trap height every 2 hours for 87 days
147 until July 15, 2010—the day of successful containment of the spill using a capping stack. The
148 release location is 28.736°N, 88.365° W at 1222 m, i.e., the estimated height of oil and gas
149 separation 300 m above the wellhead (Socolofsky et al. 2011). The oil droplets were tracked for
150 total of 167 days from the initial blowout date, and the surface oil mass (in the layer 0-1 m) and
151 the sedimented and beached oil mass were computed for each $0.1^\circ \times 0.1^\circ$ spatial bin over the
152 entire span of the oil spill. Here, oil concentrations are estimated by post-processing, and the six
153 scenarios of DSD presented in Figure 1 were carried out using two model simulations: the first
154 with oil droplets ranging from 1 to 2400 μm (case 1) and the second with oil droplets ranging

155 from 1 to 500 μm (case 2). We then computed differences in the sedimented and beached oil
156 mass and of the surface oil mass between the three scenarios of DSD for each simulation.

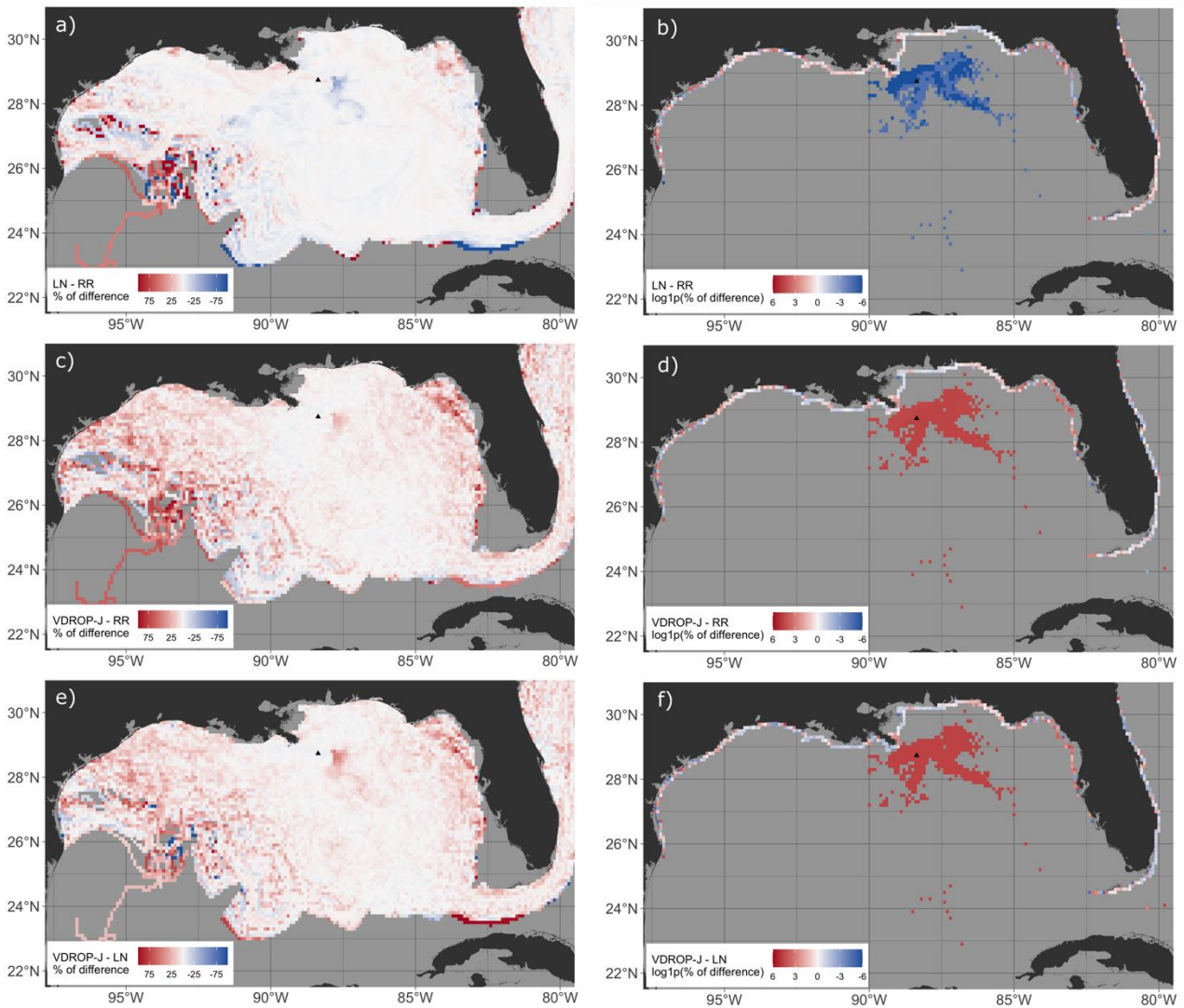
157

158 As expected, the differences are once again highly sensitive to the d_{50} and the size range of the
159 oil droplet modeled. The total combined mass of oil that beached and sedimented was indeed
160 higher by 45.29% (187,996 tons versus 129,394 tons), 43.83% (185,595 tons versus 129,038
161 tons) and 50.68% (195,052 tons versus 129,444 tons) with the smaller range of oil droplet sizes
162 and d_{50} (case 2) compared to the larger ones (case 1) for the lognormal, Rosin-Rammler and
163 VDROPI-J DSDs, respectively. Yet, the choice of the DSD's PDF played an important role
164 within each case. When comparing the proportion of oil mass that beached over the oil mass that
165 sedimented, the vast majority of the oil beached in case 1 (i.e. large d_{50}) and the choice of PDF
166 had a relatively limited influence on these outputs: only $3.2 \cdot 10^{-5}\%$ of the oil sedimented over the
167 oil that beached with the lognormal distribution, 0.1% with the Rosin-Rammler, and 1.10% with
168 the VDROPI-J distribution used here. Yet the ratios of beached versus sedimented oil mass
169 estimates for this case are far below the $21 \pm 10\%$ sedimentation rate quantified for the DWH oil
170 spill (Joye et al. 2016, Romero et al. 2017). For case 2 of the smaller oil droplets size range, this
171 ratio was reversed and the differences were closer to empirical values: the oil sedimented 2.08
172 times more than it beached with a lognormal DSD (126,978 tons sedimented vs. 61,018 tons
173 beached), 2.11 times more with a Rosin-Rammler (126,094 tons vs. 59,501 tons), and 2.32 times
174 more with the DSD modeled from VDROPI-J (136,318 tons vs. 58,735 tons). The DSD with the
175 larger d_{50} therefore predicts that almost no oil sedimented on the seafloor while most oil reached
176 the surface and then drifted to the coast, with a total mass of beached oil twice as higher
177 compared to the scenario with the smaller d_{50} . This difference also reflects high surface
178 evaporation rates (de Gouw et al. 2011), affecting mostly the largest droplets since they rise
179 faster. Interestingly, the total oil mass from case 2 that sedimented is on the same order of
180 magnitude than the oil that beached in case 1, highlighting that the predictions of oil mass
181 beached versus sedimented is critically important for evaluation response's tradeoff (Murawski
182 et al. 2019).

183

184 The proportions of beached versus sedimented oil mass on the seafloor are markedly different
185 between cases and *distribution functions* of the DSDs, but the spatial distribution of these
186 differences is perhaps more informative. With the larger droplets (case 1), the major differences
187 in surface oil concentration occur close to the blowout, 50-100 km to the ESE of the well, and at
188 the edge of the distribution in the western Gulf of Mexico, over the West Florida shelf (Figure 2,
189 left panels). The lognormal DSD leads to lower surface oil mass near the well and higher oil
190 mass in the West Bay of Louisiana compared to the Rosin-Rammler and VDRO-P-J PDFs
191 (Figure 2 and Fig. S2, left panels). The DSDs based on Rosin-Rammler and VDRO-P-J provide
192 very similar results for this size range (i.e. 1-2400 μm), with VDRO-P-J showing the highest
193 surface concentrations overall, in particular over the West Florida Shelf and western Gulf of
194 Mexico (Figure 2 and Fig. S2). Considering a Rosin-Rammler distribution instead of a
195 lognormal DSD increases the sedimentation near the blowout location, and also towards the
196 West Florida slope while it reduces the beached oil along Louisiana, Mississippi and Alabama
197 coastline (Figure 2b and Fig. S2b). Using DSD modeled from VDRO-P-J increases the
198 sedimentation of oil near the well relatively to the lognormal and Rosin-Rammler DSD, while
199 beaching increases in the western Gulf of Mexico and along the Florida Panhandle, with local
200 differences of beached oil mass of up to 641 tons per $0.1^\circ \times 0.1^\circ$ bin (*ca.* 5.9 tons/ km^2 ; Fig. S2).
201 While the overall patterns were fairly similar between the VDRO-P-J and Rosin-Rammler
202 distributions, the beaching was lower along the coast of Louisiana and Mississippi and East
203 Florida compared to the lognormal DSD in both cases, except east of the Louisiana Peninsula
204 (Figure 2b,f and Fig. S2b,f).

205



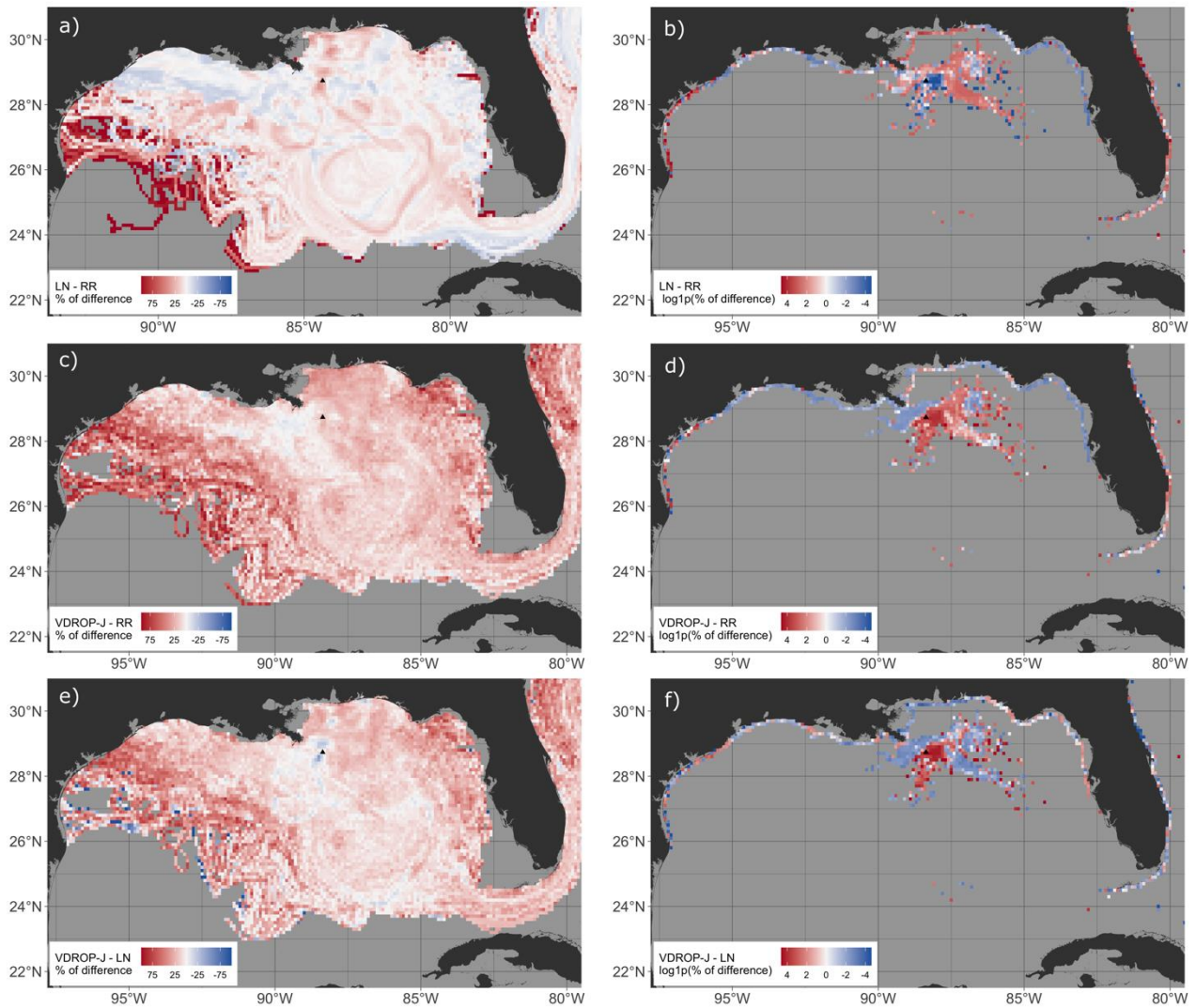
206

207 **Figure 2. (a) Maps of surface (0-1 m) oil mass differences between lognormal (LN) and**
 208 **Rosin-Rammler (RR), (c) VDROP-J and RR, (e) VDROP-J and LN, and (b) sedimented oil**
 209 **mass differences between LN and RR, (d) VDROP-J and RR, and (f) VDROP-J and LN for**
 210 **oil droplet sizes in the range 1-2400 μm (case 1) for the three DSD presented on Fig. 1a.**

211

212 The differences generated by the choice of DSD functions are more marked when considering
 213 smaller oil droplets ($< 500 \mu\text{m}$; case 2). While the proportions of differences are lower than for
 214 case 1 *per se* (generally $\leq 100\%$), the differences in the total mass of oil are considerable and
 215 surprising for the same d_{50} : up to over 400 tons of surface oil and $>4,000$ tons of sedimented oil
 216 per $0.1^\circ \times 0.1^\circ$ bins, respectively, which represents a difference of *ca.* 38.5 tons of oil per km^2
 217 (Fig. S3). Spatially, the Rosin-Rammler DSD predicts the lowest surface oil amount north of the
 218 Macondo well (Figure 3a,c). Here again, the largest relative differences occur at the edges of the

219 distribution, for each of the three DSDs. One notable difference is also found around the
220 Macondo well area, where the lognormal distribution predicts higher surface oil mass compared
221 to VDROP-J and Rosin-Rammler DSDs immediately above and up to 60 km towards the North
222 and South (Figure 3a,e). The masses of beached and sedimented oil resulting from a lognormal
223 DSD (61,019 tons and 126,989 tons, respectively) are comparable to a Rosin-Rammler
224 distribution (59,501 tons and 126,094 tons, respectively) but the spatial distribution patterns are
225 notably different: the lognormal DSD leads to increased beached oil mass in the western Gulf,
226 along the Louisiana, Mississippi, Alabama and westernmost Florida coasts, and in the domain's
227 edges (Figure 3b), and higher sedimentation in the Macondo area expect within 50 km to the east
228 of the well is lower with the latter (Figure 3b). Noteworthy differences also emerged with the
229 VDROP-J that increased sedimentation south and west of the well compared to both the
230 lognormal and Rosin-Rammler DSDs (Figure 3d,f and Fig. S3d,f). More oil beached along the
231 west coasts of the Gulf compared to the Rosin-Rammler, and both the west and east Gulf coasts
232 compared to the lognormal, while less oil reached the coasts of Louisiana and Mississippi
233 (Figure 3f and Fig. S3f). Overall, the results show that the area near the Macondo well and the
234 coastline around the Mississippi delta—the areas most impacted by the oil spill (Nixon et al.
235 2016)—are the areas where most differences emerge based on the DSD considered.



236

237 **Figure 3. (a) Maps of surface (0-1 m) oil mass differences between lognormal (LN) and**
 238 **Rosin-Rammler (RR), (c) VDROP-J and RR, (e) VDROP-J and LN, and (b) sedimented oil**
 239 **mass differences between LN and RR, (d) VDROP-J and RR, and (f) VDROP-J and LN for**
 240 **oil droplet sizes in the range 1-500 μm (case 2) for the three DSD presented on Fig. 1b.**

241

242 This study focuses on the critical choice of the DSD's PDF for modeling the transport and fate of
 243 uncontrolled deep-sea oil spills. To determine optimal oil spill responses and access tradeoffs,
 244 different scenarios are typically weighted, including considering the application of surface
 245 and/or subsea chemical dispersants (Xu et al. 2019, Murawski et al. 2019). Here, we demonstrate
 246 that, even with similar d_{50} , the surfacing time (Figure 1b,d), the distance travelled by droplets,
 247 and the patterns of sedimented and beached oil (Figure 2 & 3) will vary based on the two PDFs
 248 most frequently used for modeling the DSD during deep-sea oil spills, lognormal and Rosin-

249 Rammler (Wang and Calabrese 1986, Spaulding et al. 2015, NASEM 2019). The larger
250 divergences in patterns of surface, sedimented, and beached oil mass and ratios occur between
251 the theoretical DSDs and the modeled non-fundamental DSD from VDROF-J (Figures 1b,d,2 &
252 3). Therefore, in the absence of robust observations of the DSD in the water column, sensitivity
253 and uncertainty analyses should thus consider not only different d50, but also both of the most
254 characteristic probability distribution functions of the DSD for far-field modeling.

255

256 Differences in oil transport and fate are found between all three distributions (i.e., lognormal,
257 Rosin-Rammler, and non-fundamental VDROF-J). Our results suggest that for both d50
258 considered in cases 1 and 2, the lognormal DSD qualitatively matches better the observed
259 patterns of sedimented oil mass, with higher residual hydrocarbons in the sediment to the west
260 and north of the Macondo well and on the coasts and wetlands of Louisiana, Mississippi and
261 Alabama, and less landfall on the West Florida Shelf (Le Hénaff et al. 2012; Boufadel et al.
262 2014; Nixon et al. 2016; Romero et al. 2017). A better fit with the lognormal distribution has
263 also been suggested by laboratory (Malone et al., 2018) and field observations (Spaulding et al.,
264 2015). In conclusion, the choice of DSD function, regardless of the d50, is not trivial as it has
265 large consequences on the distribution of oil concentration in the water column, sediment and
266 shoreline. For the DWH, major differences occur at the edge of the oil distribution, which is of
267 remarkable importance since toxic oil concentrations were present in these regions, yet invisible
268 to satellite imagery (Berenshtein et al. 2020). Given the rapid advances in oil spill research
269 following DWH, extending hindcast modeling approaches to consider a range of characteristic
270 DSDs functions (d50 and PDFs) are needed to ultimately help predict the distribution of oil mass
271 and evaluating the response tradeoffs in any future deep-sea spill and response measures
272 (Malone et al. 2020, Murawski et al. 2019).

273

274 **ACKNOWLEDGEMENTS**

275 We thank the three reviewers for their thorough and helpful comments. This research was made
276 possible by a grant from the Gulf of Mexico Research Initiative (GOMRI) C-IMAGE III and

277 RECOVER2 Consortia. Data are publicly available through the Gulf of Mexico Research Initiative
278 Information and Data Cooperative (GRIIDC), DOI: [10.7266/EZYAADMS](https://doi.org/10.7266/EZYAADMS);
279 <https://data.gulfresearchinitiative.org/data/R6.x804.000:0062>.

280

281 REFERENCES

282 Aman, Z.M., Paris, C.B., May, E.F., Johns, M.L., Lindo-Atichati, D., 2015. High-pressure visual
283 experimental studies of oil-in-water dispersion droplet size. *Chem. Eng. Sci.* 127, 392–400.

284 <https://doi.org/10.1016/j.ces.2015.01.058>

285 Berenshtein, I., Paris, C.B., Perlin, N., Alloy, M.M., Joye, S.B., Murawski, S., 2020. Invisible oil
286 beyond the Deepwater Horizon satellite footprint. *Sci. Adv.* 6, 1–12.

287 <https://doi.org/10.1126/sciadv.aaw8863>

288 Boufadel, M.C., Abdollahi-Nasab, A., Geng, X., Galt, J., Torlapati, J., 2014. Simulation of the
289 landfall of the deepwater horizon oil on the shorelines of the Gulf of Mexico. *Environ. Sci.*

290 *Technol.* 48, 9496–9505. <https://doi.org/10.1021/es5012862>

291 Chan, G.K.Y., Chow, A.C., Adams, E.E., 2015. Effects of droplet size on intrusion of sub-

292 surface oil spills. *Environ. Fluid Mech.* 15, 959–973. <https://doi.org/10.1007/s10652-014-9389-5>

293 de Gouw, J.A., Middlebrook, A.M., Warneke, C., Ahmadov, R., Atlas, E.L., Bahreini, R., Blake,

294 D.R., Brock, C.A., Brioude, J., Fahey, D.W., Fehsenfeld, F.C., Holloway, J.S., Le Henaff, M.,

295 Lueb, R.A., McKeen, S.A., Meagher, J.F., Murphy, D.M., Paris, C., Parrish, D.D., Perring, A.E.,

296 Pollack, I.B., Ravishankara, A.R., Robinson, A.L., Ryerson, T.B., Schwarz, J.P., Spackman,

297 J.R., Srinivasan, A., Watts, L.A., 2011. Organic Aerosol Formation Downwind from the

298 Deepwater Horizon Oil Spill. *Science.* 331, 1295–1299. <https://doi.org/10.1126/science.1200320>

299 Delignette-Muller, M. L., Dutang, C., 2015. fitdistrplus: An R Package for Fitting Distributions.

300 *Journal of Statistical Software*, 64(4), 1-34. URL: <http://www.jstatsoft.org/v64/i04/>.

301 Gros, J., Socolofsky, S.A., Dissanayake, A.L., Jun, I., Zhao, L., Boufadel, M.C., Reddy, C.M.,

302 Arey, J.S., 2017. Petroleum dynamics in the sea and influence of subsea dispersant injection

303 during Deepwater Horizon. *Proc. Natl. Acad. Sci.* 114, 10065–10070.

304 <https://doi.org/10.1073/pnas.1612518114>

- 305 Johansen, Ø., Brandvik, P.J., and Farooq, U., 2013. Droplet breakup in subsea oil releases - Part
306 2: Predictions of droplet size distributions with and without injection of chemical dispersants.
307 *Mar. Pollut. Bull.* 73, 327-335. <https://doi.org/10.1016/j.marpolbul.2013.04.012>
- 308 Joye S.B., Bracco, A., Özgökmen, T.M., Chanton, J.P., Grosell, J.P., MacDonald, J.P. et al.
309 (2016) The Gulf of Mexico ecosystem, six years after the Macondo oil well blowout. *Deep-Sea*
310 *Res. Part II*, 129, 4-19. <https://doi.org/10.1016/j.dsr2.2016.04.018>
- 311 Le Hénaff, M., Kourafalou, V.H., Paris, C.B., Helgers, J., Aman, Z.M., Hogan, P.J., Srinivasan,
312 A., 2012. Surface evolution of the deepwater horizon oil spill patch: Combined effects of
313 circulation and wind-induced drift. *Environ. Sci. Technol.* 46, 7267–7273.
314 <https://doi.org/10.1021/es301570w>
- 315 Lehr W., Socolofsky S.A. 2020. The Importance of Understanding Fundamental Physics and
316 Chemistry of Deep Oil Blowouts. In: Murawski S. et al. (eds) *Deep Oil Spills*. Springer, Cham.
317 p. 14-24.
- 318 Li, Z., Bird, A., Payne, J., Vinhateiro, N., Kim, Y., Davis, C., Loomis, N., 2015. Technical
319 Reports for Deepwater Horizon Water Column Injury Assessment: Oil Particle Data from the
320 Deepwater Horizon Oil Spill. RPS ASA 55 Village Square Drive, South Kingstown, RI 02879.
- 321 Li, Z., Spaulding, M.L., and French-McCay, D., 2017. An algorithm for modeling entrainment
322 and naturally and chemically dispersed oil droplet size distribution under surface breaking wave
323 conditions. *Mar. Pollut. Bull.*, 119, 45-152, doi:10.1016/j.marpolbul.2017.03.048
- 324 Lindo-Atichati D, Paris C.B., Le Hénaff M., Schedler M., Valladares Juárez A.G., Müller R.,
325 2016. Simulating the effects of droplet size, high-pressure biodegradation, and variable flow rate
326 on the subsea evolution of deep plumes from the Macondo blowout, *Deep Sea Research*,
327 doi:10.1016/j.dsr2.2014.01.011
- 328 Malone, K., Aman, Z. M., Pesch, S., Schlüter, M., Krause, D., 2020. Jet formation at the spill
329 site and resulting droplet size distributions. In *Deep Oil Spills*, Springer. pp. 43-64.
- 330 Malone, K., Pesch, S., Schlüter, M., Krause, D., 2018. Oil Droplet Size Distributions in Deep-
331 Sea Blowouts: Influence of Pressure and Dissolved Gases. *Environ. Sci. Technol.* 52, 6326–
332 6333. <https://doi.org/10.1021/acs.est.8b00587>

- 333 Murawski, S.A., Schlüter, M., Paris, C.B., Aman, Z.M., 2019. Resolving the dilemma of
334 dispersant use for deep oil spill response. *Environ. Res. Lett.* 14, 091002.
335 <https://doi.org/10.1088/1748-9326/ab3aa0>
- 336 National Academies of Sciences and Medicine, E., 2019. *The Use of Dispersants in Marine Oil*
337 *Spill Response*. The National Academies Press, Washington, DC.
338 <https://doi.org/10.17226/25161>
- 339 Nixon Z, Zengel S, Baker M, Steinhoff M, Fricano G, Rouhani S, et al. Shoreline oiling from the
340 Deepwater Horizon oil spill. *Mar Pollut Bull.* 2016; 107: 170–178.
341 doi:10.1016/j.marpolbul.2016.04.003
- 342 Paris, C.B., Berenshtein, I., Trillo, M.L., Faillettaz, R., Olascoaga, M.J., Aman, Z.M., Schlüter,
343 M., Boye, S. B., 2018. BP Gulf Science Data Reveals Ineffectual Subsea Dispersant Injection for
344 the Macondo Blowout. *Front Mar Sci.* 5:389. doi:10.3389/fmars.2018.00389
- 345 Paris, C.B., Le Hénaff, M., Aman, Z.M., Subramaniam, A., Helgers, J., Wang, D.-P.,
346 Kourafalou, V.H., Srinivasan, A., 2012. Evolution of the Macondo Well Blowout: Simulating
347 the Effects of the Circulation and Synthetic Dispersants on the Subsea Oil Transport. *Environ.*
348 *Sci. Technol.* 46, 13293–13302. <https://doi.org/10.1021/es303197h>
- 349 Paris, C.B., Helgers, J., van Sebille, E., Srinivasan, A., 2013. Connectivity Modeling System: A
350 probabilistic modeling tool for the multi-scale tracking of biotic and abiotic variability in the
351 ocean. *Environ. Model. Softw.* 42, 47–54. <https://doi.org/10.1016/j.envsoft.2012.12.006>
- 352 Perlin, N., Paris, C.B., Berenshtein, I., Vaz, A.C., Faillettaz, R., Aman, Z.M., Schwing, P.T.,
353 Romero, I.C., Schlüter, M., Liese, A., 2020. Far-Field Modeling of a Deep-Sea Blowout:
354 Sensitivity Studies of Initial Conditions, Biodegradation, Sedimentation, and Subsurface
355 Dispersant Injection on Surface Slicks and Oil Plume Concentrations, in: *Deep Oil Spills*.
356 Springer, pp. 170–192.
- 357 Pesch, S.; Jaeger, P.; Jaggi, A.; Malone, K.; Hoffmann, M.; Krause, D.; Oldenburg, T.B.P.;
358 Schlüter, M., 2018. Rise Velocity of Live-Oil Droplets in Deep-Sea Oil Spills. *Env. Engine. Sci.*
359 35 (4), 289–299.

- 360 Pesch S, Knopf R, Radmehr A, Paris CB, and Aman ZM, Hoffmann M, Schlüter M. 2020a
361 Experimental investigation, scale-up and modeling of droplet size distributions in turbulent
362 multiphase jets, *Multiphase Science and Technology*, 32(2):113–136
- 363 Pesch, S.; Schlüter, M.; Aman, Z.M.; Malone, K.; Krause, D.; Paris, C.B., 2020b. Behavior of
364 Rising Droplets and Bubbles: Impact on the Physics of Deep-Sea Blowouts and Oil Fate. In:
365 Murawski, S.A.; Ainsworth, C.H.; Gilbert, S.; Hollander, D.J.; Paris, C.B.; Schlüter, M.; Wetzel,
366 D.L. (eds.). *Deep Oil Spills – Facts, Fate and Effects*. Springer Nature Switzerland, 65–82.
- 367 Romero, I.C., Toro-Farmer, G., Diercks, A.R., Schwing, P., Muller-Karger, F., Murawski, S.,
368 Hollander, D.J., 2017. Large-scale deposition of weathered oil in the Gulf of Mexico following a
369 deep-water oil spill. *Environ. Pollut.* 228, 179–189. <https://doi.org/10.1016/j.envpol.2017.05.019>
- 370 Ryerson, T.B., Camilli, R., Kessler, J.D., Kujawinski, E.B., Reddy, C.M., Valentine, D.L., Atlas,
371 E., Blake, D.R., De Gouw, J., Meinardi, S., Parrish, D.D., Peischl, J., Seewald, J.S., Warneke, C.,
372 2012. Chemical data quantify Deepwater Horizon hydrocarbon flow rate and environmental
373 distribution. *Proc. Natl. Acad. Sci. U. S. A.* 109, 20246–20253.
374 <https://doi.org/10.1073/pnas.1110564109>
- 375 Socolofsky, S.A., Adams, E.E., Boufadel, M.C., Aman, Z.M., Johansen, Ø., Konkel, W.J.,
376 Lindo, D., Madsen, M.N., North, E.W., Paris, C.B., Rasmussen, D., Reed, M., Rønningen, P.,
377 Sim, L.H., Uhrenholdt, T., Anderson, K.G., Cooper, C., Nedwed, T.J., 2015. Intercomparison of
378 oil spill prediction models for accidental blowout scenarios with and without subsea chemical
379 dispersant injection. *Mar. Pollut. Bull.* 96, 110–126.
380 <https://doi.org/10.1016/j.marpolbul.2015.05.039>
- 381 Socolofsky, S.A., Adams, Sherwood, C.R., 2011. Formation dynamics of subsurface
382 hydrocarbon intrusions following the Deepwater Horizon blowout, *Geophy. Res. Lett.*, 8,
383 L09602, doi:10.1029/2011GL047174, 2011
- 384 Socolofsky, S.A., Gros, J., North, E., Boufadel, M.C., Parkerton, T.F., Adams, E.E., 2019. The
385 treatment of biodegradation in models of sub-surface oil spills: A review and sensitivity study.
386 *Mar. Pollut. Bull.* 143, 204–219. <https://doi.org/10.1016/j.marpolbul.2019.04.018>
- 387 Spaulding, M., Li, Z., Mendelsohn, D., Crowley, D., French-McCay, D., Bird, A., 2017.
388 Application of an Integrated Blowout Model System, OILMAP DEEP, to the Deepwater

- 389 Horizon (DWH) Spill. *Mar. Pollut. Bull.* 120, 37–50.
390 <https://doi.org/10.1016/j.marpolbul.2017.04.043>
- 391 Spaulding, M., Mendelsohn, D., Crowley, D., Li, Z., Bird, A., 2015. DRAFT Technical Reports
392 for Deepwater Horizon Water Column Injury Assessment.
- 393 Tambe, D.E., Sharma, M.M., 1994. The effect of colloidal particles on fluid-fluid interfacial
394 properties and emulsion stability. *Adv. Colloid Interface Sci.* 52, 1–63.
395 [https://doi.org/10.1016/0001-8686\(94\)80039-1](https://doi.org/10.1016/0001-8686(94)80039-1)
- 396 Testa, J.M., Eric Adams, E., North, E.W., He, R., 2016. Modeling the influence of deep water
397 application of dispersants on the surface expression of oil: A sensitivity study. *J. Geophys. Res.*
398 *Ocean.* 121, 5995–6008. <https://doi.org/10.1002/2015JC011571>
- 399 Wang, C.Y., Calabrese, R. V., 1986. Drop breakup in turbulent stirred- tank contactors. Part II:
400 Relative influence of viscosity and interfacial tension. *AIChE J.* 32, 667–676.
401 <https://doi.org/10.1002/aic.690320417>
- 402 Xu, C., Lin, P., Zhang, S., Sun, L., Xing, W., Schwehr, K.A., Chin, W.-C., Wade, T.L., Knap,
403 A.H., Hatcher, P.G., Yard, A., Jiang, C., Quigg, A., Santschi, P.H., 2019. The interplay of
404 extracellular polymeric substances and oil/Corexit to affect the petroleum incorporation into
405 sinking marine oil snow in four mesocosms. *Sci. Total Environ.* 693, 133626.
406 <https://doi.org/10.1016/j.scitotenv.2019.133626>
- 407 Zhao, L., Shaffer, F., Robinson, B., King, T., D'Ambrose, C., Pan, Z., Gao, F., Miller, R.S.,
408 Conmy, R.N., Boufadel, M.C., 2016. Underwater oil jet: Hydrodynamics and droplet size
409 distribution. *Chem. Eng. J.* 299, 292–303. <https://doi.org/10.1016/j.cej.2016.04.061>
- 410 Zhao L, Boufadel MC, Socolofsky SA, Adams E, King T, Lee K. Evolution of droplets in subsea
411 oil and gas blowouts: Development and validation of the numerical model VDROD-J. *Mar Pollut*
412 *Bull.* 2014;83: 58–69. doi:10.1016/j.marpolbul.2014.04.020
- 413 Zheng L, Yapa PD. 2000. Buoyant velocity of spherical and nonspherical bubbles/droplets. *J*
414 *Hydraul Eng.*;126: 852–854.
- 415 Zheng, L., Yapa, P.D., Chen, F., 2003. A model for simulating deepwater oil and gas blowouts -
416 Part I: Theory and model formulation. *J. Hydraul. Res.* 41, 339–351.

This work is licensed under a [CC-BY-NC-ND 4.0 license](https://creativecommons.org/licenses/by-nc-nd/4.0/).

18

Faillettaz et al. 2021 – Marine Pollution Bulletin – doi : [10.1016/j.marpolbul.2020.111920](https://doi.org/10.1016/j.marpolbul.2020.111920)